PNAS RESEARCH ARTICLE | BIOCHEMISTRY

Dual factors required for cytochrome-P450-mediated hydrocarbon ring contraction in bacterial gibberellin phytohormone biosynthesis

Raimund Nagel[a,1], Liza E. Alexander[a,2], Charles E. Stewart Jr.[b], and Reuben J. Peters[a,3]

Edited by Harry Gray, California Institute of Technology, Pasadena, CA; received December 19, 2022; accepted May 2, 2023

Cytochromes P450 (CYPs) are heme-thiolate monooxygenases that prototypically catalyze the insertion of oxygen into unactivated C–H bonds but are capable of mediating more complex reactions. One of the most remarked-upon alternative reactions occurs during biosynthesis of the gibberellin A (GA) phytohormones, involving hydrocarbon ring contraction with coupled aldehyde extrusion of *ent*-kaurenoic acid to form the first gibberellin intermediate. While the unusual nature of this reaction has long been noted, its mechanistic basis has remained opaque. Building on identification of the relevant CYP114 from bacterial GA biosynthesis, detailed structure–function studies are reported here, including development of in vitro assays as well as crystallographic analyses both in the absence and presence of substrate. These structures provided insight into enzymatic catalysis of this unusual reaction, as exemplified by identification of a key role for the "missing" acid from an otherwise highly conserved acid–alcohol pair of residues. Notably, the results demonstrate that ring contraction requires dual factors, both the use of a dedicated ferredoxin and absence of the otherwise conserved acidic residue, with exclusion of either limiting turnover to just the initiating and more straightforward hydroxylation. The results provide detailed insight into the enzymatic structure–function relationships underlying this fascinating reaction and support the use of a semipinacol mechanism for the unusual ring contraction reaction.

enzymatic structure–function | monooxygenase | reaction mechanism

Cytochromes P450 (CYPs) form a highly diverse enzymatic superfamily (1), with only the cysteinate heme-iron ligand exhibiting universal conservation (2). Their activity relies on this prosthetic group, most often to catalyze the energetically difficult insertion of oxygen into unactivated C–H bonds (3). This basic activity stems from the activation of molecular dioxygen via a catalytic cycle involving not only binding of substrate and dioxygen, but also reduction via electrons generally obtained from nicotinamide adenine dinucleotide phosphate (NADPH) via a separate redox partner. Notably, the resulting ferryl-oxo radical cation (termed Compound I) (4) is highly reactive and has been likened to a "blowtorch" (5).

The typical CYP catalytic cycle begins in the resting low-spin ferric (Fe^{3+}) state, with a water serving as the "sixth" Fe ligand. This is displaced by substrate binding, converting the iron to a high-spin state, which exhibits altered spectral properties (6). The change in Fe spin state also alters its redox potential, enabling reduction to the ferrous (Fe^{2+}) form, with the electron generally supplied by a separate redox partner (7). The reduced Fe^{2+} then binds dioxygen, forming a ferric-superoxide species, and triggering a second reduction to form a ferric-peroxo species. This undergoes consecutive addition of two protons, assisted by a highly conserved acid–alcohol pair of residues (8), with the first protonation yielding a ferric-hydroperoxo species termed Compound 0, while the second leads to heterolytic cleavage, releasing H_2O and forming the typically utilized Compound I (4). This ferryl-oxo species usually abstracts a proximal hydrogen from the substrate, with subsequent radical recombination yielding a hydroxyl group in what has been termed the oxygen rebound mechanism (8). In addition to this physiologically relevant catalytic cycle, it has been found that CYPs can use exogenous oxidants to bypass early stages (9), with hydrogen peroxide (H_2O_2) generally forming Compound 0, while *tert*-butyl hydroperoxide (*t*BuOOH) directly yields Compound I (*SI Appendix*, Fig. S1).

Beyond the prototypical hydroxylation reaction, CYPs are capable of catalyzing more unusual transformations, although the basis for many of these is not well understood (10). Arguably most interesting are those modifying the underlying backbone structure (11). Among these, the ring contraction required for production of gibberellin A (GA) phytohormones has long been cited as a particularly intriguing example, albeit with unknown mechanism (12). This reaction transforms the 6–6–6–5 hydrocarbon tetracycle of its *ent*-kaurenoic acid (KA) substrate to the 6–5–6–5 ring structure characterizing the

Significance

Cytochromes P450 (CYPs) are versatile monooxygenases that usually catalyze hydroxylation reactions, but can mediate more complex reactions. The enzymatic structure–function relationships underlying such unusual activity are of significant interest, given both the biological importance of these transformations and potential insight into reverse engineering such catalysis. Here, detailed insight is provided into CYP114, which catalyzes the hydrocarbon ring contraction defining gibberellin phytohormone biosynthesis in certain plant-associated bacteria. The results define dual factors, both interaction with a specific (ferredoxin) redox partner and the absence of the usual acidic residue from an otherwise highly conserved acid–alcohol pair, required for CYP114 to mediate the unusual ring contraction reaction, via a semipinacol mechanism, with restriction to just the initiating hydroxylation otherwise observed.

The authors declare no competing interest.

This article is a PNAS Direct Submission.

[1]Present address: Department of Plant Physiology, Institute of Biology, Leipzig University, D-04103 Leipzig, Germany.

[2]Present address: Assay Development, Pattern Bioscience, Austin, TX 78752.

[3]To whom correspondence may be addressed. Email: rjpeters@iastate.edu.

This article contains supporting information online at https://www.pnas.org/lookup/suppl/doi:10.1073/pnas.2221549120/-/DCSupplemental.

Published June 20, 2023.

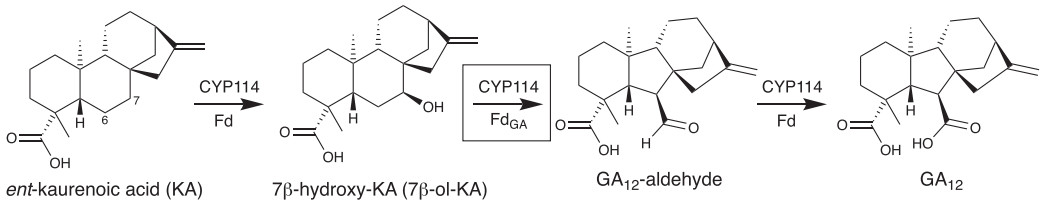

Scheme 1. CYP114 catalyzed reactions, from (initial) C-7β hydroxylation of *ent*-kaurenoic acid (KA) catalyzed in the presence of most ferredoxin (Fd), to subsequent unusual ring contraction reaction catalyzed specifically with Fd$_{GA}$ (boxed), and further oxidation to GA$_{12}$ catalyzed (albeit inefficiently) in the presence of most Fd.

gibberellins, with concurrent extrusion of carbon-7 (C-7) as an aldehyde, forming GA$_{12}$-aldehyde (13).

Strikingly, bioactive GA can affect plant–microbe interactions (14), which has led to the production of these structurally complex phytohormones by certain plant-associated microbes, both fungi and bacteria (13). While the transformations in each pathway are essentially identical in plants and bacteria, and the fungal pathway differs in only the order of occurrence of a peripheral (C-3β) hydroxylation step, the relevant enzymes exhibit very low (in some cases no) homology, indicating that each kingdom independently evolved such biosynthetic capacity. For example, the CYPs catalyzing the ring contraction reaction fall into different families (CYP88 in plants, CYP68 in fungi, and CYP114 in bacteria), between which there is less than 15% amino acid sequence identity (15). Moreover, while eukaryotic CYPs contain N-terminal transmembrane helices, bacterial CYPs do not and, thus, are soluble (7)—e.g., CYP88 and CYP68 versus CYP114. In addition, these differ in terms of redox partners, with eukaryotic CYPs generally pairing with cytochrome P450 reductases (CPRs), while bacterial CYPs typically obtain their electrons from ferredoxins (Fd) that are, in turn, reduced by Fd–NADPH reductases (7).

Notably, the redox partner can vary and affect CYP catalysis (7). A well-known example of this is found with CYP17A1, which catalyzes a steroidal 17α-hydroxylation reaction in conjunction with the usual CPR redox partner, but also pairs with cytochrome-b_5 to subsequently mediate an unusual 17,20-lyase reaction (16). Of particular relevance here, CYP114 requires a dedicated Fd also found in the bacterial GA biosynthetic operon (Fd$_{GA}$) to mediate the ring contraction reaction (15). In the recombinant whole-cell feeding assays to which previous studies have been limited, in the absence of Fd$_{GA}$, CYP114 catalyzes only C-7β-hydroxylation (Scheme 1), presumably partnering with an endogenous Fd (15, 17–20). The resulting 7β-hydroxy-KA (7β-ol-KA) can serve as an intermediate and be exogenously utilized by either native bacteroids (15), or exogenously expressed bacterial CYP114 + Fd$_{GA}$, albeit quite inefficiently and with only a single example of such recombinant activity (18).

Results

Here, the CYP114 from *Erwinia tracheiphila* was chosen for more detailed studies, as it is in the same *Enterobacteriaceae* family as *Escherichia coli* and is readily overexpressed therein. This *Et*CYP114 retained full activity with an N-terminal His-tag, as indicated by the ability of recombinant *E. coli* coexpressing this with the corresponding *Et*Fd$_{GA}$ to convert KA to GA$_{12}$-aldehyde, as well as the further oxidized GA$_{12}$ (Fig. 1*A*), just as previously observed with untagged constructs (18). Moreover, this tagged version of *Et*CYP114 was readily overexpressed and could be purified in a functionally folded form, as indicated by observation of the eponymous peak at 450 nm in carbon monoxide–binding spectra (*SI Appendix*, Fig. S2*A*). Unfortunately, it was not possible to carry out in vitro assays with *Et*Fd$_{GA}$, as no activity was observed, even with recombinant cell extracts. This appears to be due to oxygen sensitivity of *Et*Fd$_{GA}$, as the spectral features associated with the iron–sulfur cluster were only observed following purification under anaerobic conditions and were immediately lost upon exposure to oxygen (*SI Appendix*, Fig. S2*B*). Consistent with the specific requirement for Fd$_{GA}$ to enable the ring contraction reaction (18), when the commercially available spinach Fd was used as a redox partner for in vitro reactions, *Et*CYP114 only catalyzes conversion of KA to 7β-ol-KA (Fig. 1*B*).

In an attempt to produce a protein that can catalyze the ring contraction reaction in vitro, based on the observation of naturally occurring fusions between CYP114 and Fd$_{GA}$ (21, 22), an analogous fusion was constructed here with *Et*CYP114 and *Et*Fd$_{GA}$. While this fused *Et*CYP114–Fd$_{GA}$ construct also was not functional in vitro, the activity observed upon feeding KA to the resulting recombinant culture was notably more restricted. In particular, cultures expressing *Et*CYP114–Fd$_{GA}$ yielded essentially exclusively GA$_{12}$-aldehyde (*SI Appendix*, Fig. S3*A*). Given that fusion presumably enforces interaction between the tethered CYP and Fd (i.e., *Et*CYP114 and *Et*Fd$_{GA}$), this suggests that further oxidation of GA$_{12}$-aldehyde to GA$_{12}$ relies on the use of alternate redox partners. This is analogous to the use of endogenous Fd that enables CYP114 to produce (only) 7β-ol-KA in the absence of Fd$_{GA}$ (18). Consistent with this hypothesis, whole-cell feeding studies with *E. coli*-expressing *Et*CYP114 alone demonstrated that this is sufficient for conversion of GA$_{12}$-aldehyde to GA$_{12}$ (*SI Appendix*, Fig. S3*B*). By contrast, analogous whole-cell feeding studies with the fused *Et*CYP114–Fd$_{GA}$ construct demonstrated only trace conversion of GA$_{12}$-aldehyde to GA$_{12}$.

To enable in vitro assays, the Fd$_{GA}$ from *Bradyrhizobium japonicum* (*Bj*Fd$_{GA}$) was examined and found to be aerobically stable as indicated by its UV–Vis spectra, even upon reduction with dithionite (*SI Appendix*, Fig. S4). Whole-cell feeding studies indicated that *Bj*Fd$_{GA}$ can partner with *Et*CYP114 (either as a separate protein or in the context of a fused polypeptide) to drive ring contraction, albeit the formation of GA$_{12}$ (particularly by the fused *Et*CYP114–*Bj*Fd$_{GA}$) suggests that their interaction is not as efficient at restricting this activity as the native pairing (*SI Appendix*, Fig. S5). Nevertheless, use of *Bj*Fd$_{GA}$ enabled the conversion of KA to GA$_{12}$-aldehyde and GA$_{12}$ by *Et*CYP114 in vitro. Consistent with reduced efficiency of the interaction between *Et*CYP114 and *Bj*Fd$_{GA}$, substantial amounts of 7β-ol-KA were produced as well (*SI Appendix*, Fig. S6*A*). Unlike the previously reported ability of *Et*CYP114 + *Et*Fd$_{GA}$ to catalyze (albeit inefficiently) ring contraction with 7β-ol-KA in whole-cell assays (18), these in vitro assays were inconsistent and showed either no or only trace conversion of 7β-ol-KA to GA$_{12}$-aldehyde (*SI Appendix*, Fig. S6*B*), emphasizing the transient nature of this intermediate. Regardless, while the interaction between *Et*CYP114 and *Bj*Fd$_{GA}$ may not be optimal, these experiments demonstrate that Fd$_{GA}$ is sufficient for catalysis of the ring contraction reaction by CYP114, acting not only as a redox partner but also to alter activity, enabling catalysis of the ring contraction reaction.

Purification of *Et*CYP114 enabled examination of its substrate specificity through UV–Vis spectral binding studies. *Et*CYP114 exhibited typical Type I–binding spectra with KA, although there was incomplete (~50%) conversion of the Soret band to the

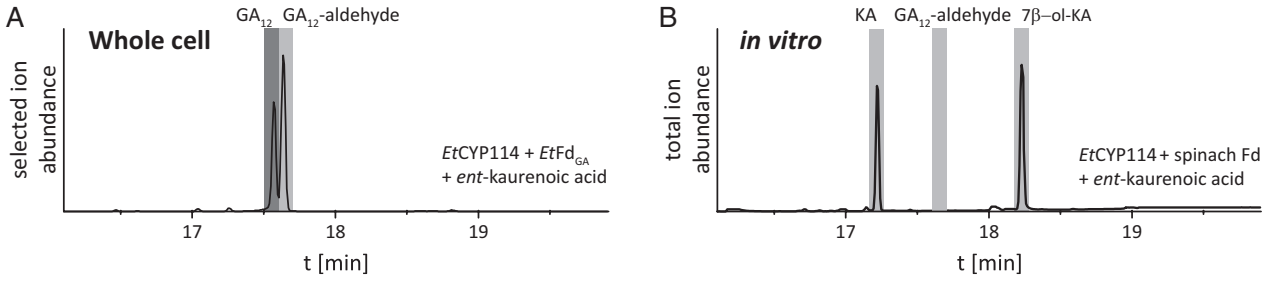

Fig. 1. CYP114 catalyzed ring contraction reaction. (*A*) GC–MS chromatogram from organic extracts of *E. coli* cultures expressing His-tagged *Et*CYP114 and *Et*Fd$_{GA}$, and fed *ent*-kaurenoic acid (KA). (*B*) GC–MS chromatogram of in vitro enzyme assays with *Et*CYP114, spinach Fd, ferredoxin reductase, NADPH, and KA (7β-ol-KA, 7β-hydroxy-*ent*-kaurenoic acid).

high-spin state (*SI Appendix*, Fig. S7*A*), suggesting dynamic equilibrium with the low-spin state. Nevertheless, quite tight binding was observed, with the measured K_d = 65 ± 7 nM (*SI Appendix*, Fig. S7*B*). By contrast, very little binding was observed for even closely related analogs (*SI Appendix*, Fig. S8). For example, of the upstream intermediates, only *ent*-kaurenal, which in its more prevalent *gem*-diol form sterically resembles KA, induces a relatively small decrease in the Soret band (~10%) and no change in the α-band, with a ~1,000-fold decrease in affinity relative to KA (K_d = 70 ± 14 μM), while *ent*-kaurene, *ent*-kaurenol, and methylated *ent*-kaurenoate do not induce consistent changes in absorption at these bands. This emphasizes the importance of the carboxylate moiety for substrate binding. Notably, 7β-ol-KA induced only a minor decrease in the Soret band, although no decrease in the α-band, but only a modest decrease in affinity, as determined by competitive titration against KA (K_i ~ 0.4 μM).

To provide more detailed insight into substrate binding and activity, crystal structures were determined for *Et*CYP114, both in the absence (apo) and presence of KA (*SI Appendix*, Table S1). The apo structure of *Et*CYP114 was solved by molecular replacement at a resolution of 1.68 Å in space group $C222_1$ and resembles that of other previously characterized CYPs, containing both the B and B′ helices (23). *Et*CYP114 also was cocrystallized with KA in two distinct space groups. Both diffracted to high resolution (1.70 Å and 1.83 Å), and exhibited minimal differences, with C_a RMSD = 0.33 Å (*SI Appendix*, Fig. S9). Moreover, in both crystal forms, *Et*CYP114 has identical contacts to the bound KA (*SI Appendix*, Fig. S10), providing additional confidence in the observed interactions. There are the expected changes between the apo- and substrate-bound *Et*CYP114 structures (C_a RMSD = 2.9 Å), with the largest movements found in the F and G helices, as well as intervening loop, which moves ~7 to 8 Å (Fig. 2*A*). Together, these movements close the substrate access channel and completely encase the substrate (*SI Appendix*, Fig. S11).

The orientation of the bound KA substrate appears to be catalytically relevant, with the C-7β hydrogen closest to the heme iron (3.7 Å) and appropriately positioned for catalysis (C–H bond approximately parallel with heme plane), with the C-6β hydrogen that additionally must be acted upon for ring contraction the next closest (3.9 Å), while all other are ≥5 Å away (Fig. 2*B*). Most of the interactions between *Et*CYP114 and KA are hydrophobic in nature (Fig. 2*C* and *SI Appendix*, Figs. S10 and S11). These are mediated by the side chains of residues from the B′-helix (Leu94), following loop (Thr97, Leu98, and Ala99), F-helix (Leu187 and Leu190), I-helix (Trp253, Gly254, Ile255, Leu257, Gly258, and Thr262), loop after the K-helix (Ala305 and Ile310), and flexible region in the C terminus (Phe417 and Leu418), as well as the heme. Given the importance of the carboxylate moiety for binding noted above, there are surprisingly few contacts to this functional group. In fact, only two hydrogen bonds. These are to the hydroxyl group of the side chain in Ser308 and the backbone nitrogen of Ser309, both of which are part of the loop after the K-helix.

Notably, a cluster of three well-defined waters are found in the active site near the heme-Fe in the substrate-bound structures (*SI Appendix*, Fig. S12). All the three waters are hydrogen bound to the side-chain hydroxyl of a threonine (T262), which is normally part of a highly conserved acid–alcohol adjacent pair of residues (generally Asp followed by Thr), that prototypically activate such proximal water to serve as the source of the protons required for the typical catalytic cycle (24). Intriguingly, the

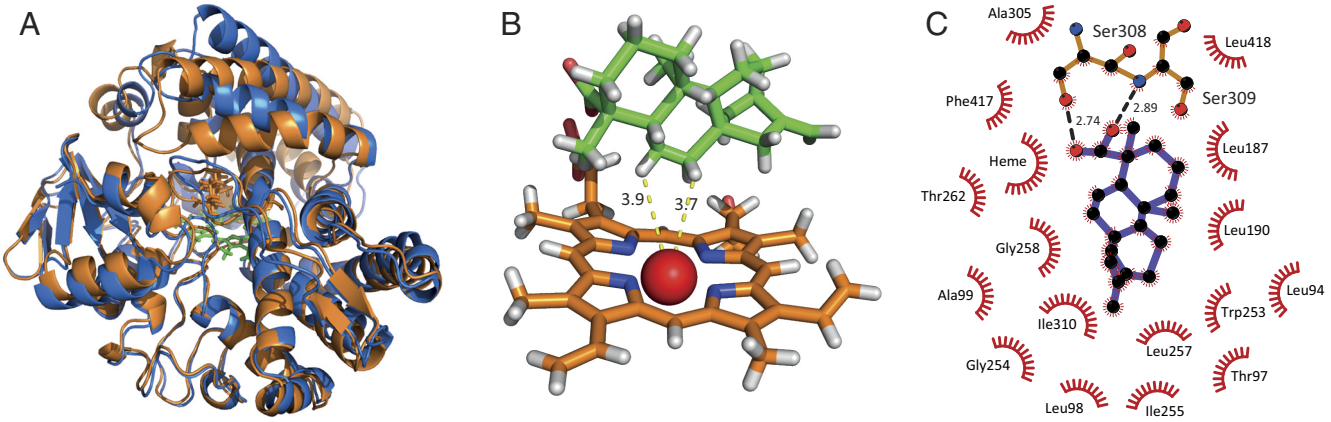

Fig. 2. Overlay of the crystal structure of apo and substrate-bound *Et*CYP114. (*A*) The structures were overlaid in Coot and visualized as cartoon models in PyMol. The apo-structure is shown in blue and the substrate-bound structure from Crystal Form 1 ($P2_12_12_1$) is shown in orange; for clarity, the heme is shown in green for both. The RMSD between the C_a-backbones was calculated in Coot as 2.9 Å. (*B*) Orientation of *ent*-kaurenoic acid (green) relative to heme-iron (orange-red), with distances shown to C-7β hydrogen reacted upon for initial hydroxylation and C-6β hydrogen targeted in the subsequent ring contraction reaction. (*C*) Interaction map of *ent*-kaurenoic acid with *Et*CYP114 in Crystal Form 1 (generated with LigPlot+, with hydrophobic interactions up to a distance of 5 Å included).

preceding residue is no longer acidic in all CYP114 and is generally an Ala (e.g., A261 in *Et*CYP114), with only Val found otherwise. Given lack of this otherwise conserved acid–alcohol pair has been associated with alternative reactivity (25), the importance of this unusual CYP114 conservation pattern was investigated in *Et*CYP114 via substitution of Asp for this Ala. Strikingly, whole-cell feeding studies with the resulting A261D mutant of *Et*CYP114, even in the presence of *Et*Fd_{GA} (expressed either separately or in the context of an *Et*CYP114–Fd_{GA} fusion construct), only led to the production of 7β-ol-KA (Fig. 3)—i.e., *Et*CYP114:A261D cannot catalyze the ring contraction reaction and is limited to 7β-hydroxylation.

These results suggest the mechanistic hypothesis that introduction of this acidic residue enables protonation of the dioxygen to generate Compound I and, hence enable activity. This was further examined via the use of exogenous oxidants to directly generate Compound 0 (H_2O_2) or Compound I (*t*BuOOH) of the typical CYP catalytic cycle (9). Consistent with an inability to carry out dioxygen protonation, *Et*CYP114 is not reactive with H_2O_2, but can catalyze 7β-hydroxylation with *t*BuOOH—i.e., only upon direct generation of Compound I (*SI Appendix*, Fig. S13 *A* and *B*). Critically, although *Et*CYP114:A261D exhibits ~fivefold reduced affinity for KA (K_d = 320 ± 34 nM), with very little (<10%) shift to a high-spin state (*SI Appendix*, Fig. S14), it is reactive with not only *t*BuOOH, but also H_2O_2, with both leading to production of 7β-ol-KA (*SI Appendix*, Fig. S13 *C* and *D*). Accordingly, introduction of this acidic residue appears to be sufficient to impart the ability to mediate at least protonation of Compound 0 (as generated by H_2O_2) to form Compound I and enable catalysis.

Although whole-cell feeding studies of *Et*CYP114:A261D with KA in the presence of *Bj*Fd_{GA} indicated catalysis of ring contraction (*SI Appendix*, Fig. S15), in vitro assays of *Et*CYP114:A261D with *Bj*Fd_{GA} demonstrated that 7β-hydroxylation was the predominant product, with <10% of the reactions leading to ring contraction—i.e., yielding GA_{12}-aldehyde and, subsequently, GA_{12} (*SI Appendix*, Fig. S16). To further understand the role of this restoration of the acid–alcohol motif, the crystal structure of *Et*CYP114:A261D was solved at 2.6 Å (*SI Appendix*, Fig. S17). In comparison to *Et*CYP114, the mutant showed only minimal differences in the overall structure, with C_α RMSD = 0.477 Å and overall RMSD of 0.979 Å (*SI Appendix*, Fig. S18), although the introduced carboxylate is hydrogen bonded to water that is not present in the wild-type structure.

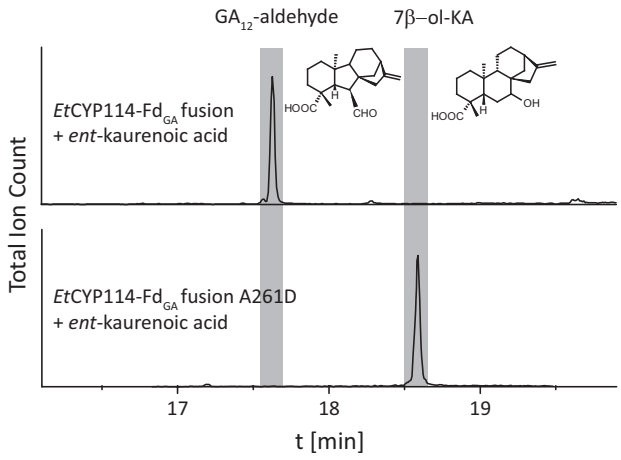

Fig. 3. The acid–alcohol motif influences product outcome. GC-chromatograms of organic extracts of *E. coli* cultures expressing the *Et*CYP114–Fd_{GA} fusion, either the wild type or A261D mutant, after *ent*-kaurenoic acid was added to the culture as substrate.

Discussion

The results reported here provide insight into the notably unusual ring contraction reaction catalyzed by CYP114 in bacterial GA biosynthesis. Indeed, the *Et*CYP114 crystal structures reported here provide the first atomic-level view into any oxidative enzyme involved in gibberellin biosynthesis from bacteria, fungi, or plants. As expected, the complex of CYP114 and its substrate KA is consistent with the catalyzed reactions, particularly initial hydroxylation at the C-7β position, with the C-6β hydrogen presumably extracted in the ring contraction reaction also falling within the usual reactive range from the heme-iron active center.

Notably, it is now clear that the ring contraction reaction catalyzed by CYP114 relies not only on interaction with the dedicated Fd_{GA}, as clarified by the in vitro assays developed here, but also the "absence" of an otherwise conserved acidic residue discovered here. In particular, as either use of other Fd or "restoration" of this key acidic residue (A261D) is sufficient to essentially limit *Et*CYP114 activity to 7β-hydroxylation. Indeed, the importance of the complex between CYP114 and Fd_{GA} for catalysis of the ring contraction reaction is consistent with the ability of the fused native redox pair *Et*CYP114–Fd_{GA} to restrict reactivity beyond this transformation—i.e., production of GA_{12}-aldehyde without further oxidation to GA_{12}. Thus, these dual factors are required for CYP114 to catalyze the unusual ring contraction reaction.

Intriguingly, the notable lack of ionic interactions with the carboxylate moiety of KA is consistent with the previously hypothesized importance of the associated negative charge for the ring contraction reaction, which potentially provides anchimeric assistance (20). However, despite the obvious chemical similarities, this moiety cannot serve as a substitute for the absence of the otherwise conserved acidic residue (i.e., activating water for protonation of iron–dioxygen species), as it is located on the opposite side of the substrate and does not interact with water in any case. Instead, as indicated by the striking conservation of this transformation in biosynthesis of gibberellin phytohormones in the independently evolved pathways from plants, fungi, and bacteria, the carboxylate moiety of KA has been suggested to support the use of a carbocation-based (semi)pinacol (beyond the usual radical) mechanism for the ring contraction reaction (20). It has since been shown that CYP114 does not react with 6β,7β-dihydroxy-KA, the intermediate for a pinacol mechanism, although this is found as a minor side product (18). CYP114 also does not react with 7β-hydroxy-*ent*-kaurenolide, the covalent intermediate expected from more direct (covalent) anchimeric assistance in a semipinacol mechanism (18, 20). Accordingly, while a more traditional radical-mediated mechanism for this unusual ring contraction reaction cannot be ruled out, it seems most likely that the carboxylate moiety of KS provides ionic pairing to stabilize the C-6 carbocation in a semipinacol mechanism (Scheme 2).

How absence of the otherwise conserved acidic residue and required interaction with Fd_{GA} enables catalysis of the ring contraction reaction remains unclear. Nevertheless, it has been shown in other CYP systems that redox partner binding alters the conformation and hydrogen-bonding network of exactly this residue (24). Indeed, given initial hydroxylation can be accomplished in the presence of a variety of Fd, such interaction is sufficient to enable use of the usual CYP catalytic cycle, including dioxygen protonation. Thus, it could be that the introduction of Asp simply blocks the reactive binding orientation for 7β-ol-KA otherwise enabled by the interaction with Fd_{GA}. More specifically, given the impact of this mutation on dioxygen protonation in the CYP catalytic cycle, its ability to block the ring contraction reaction

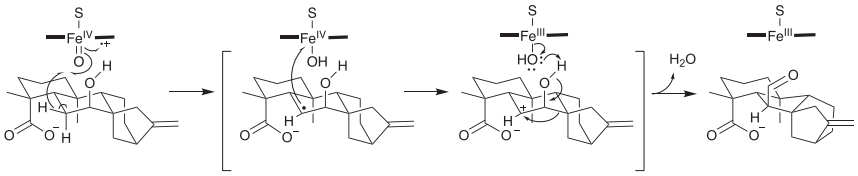

Scheme 2. Proposed semipinacol mechanism for the ring contraction reaction, proceeding via hydrogen abstraction from C-6β and, subsequently, transfer of the unpaired electron to the heme-iron, with rearrangement of the resulting C-6 carbocation leading to aldehyde extrusion.

might stem from altering the hydrogen-bonding network, including configuration of waters, within the active site.

Regardless, the detailed studies reported here provide enzymatic structure–function insights into the ring contraction reaction representing the committed step in GA biosynthesis. Not least that catalysis of this unusual reaction by the bacterial CYP114 family members depends on dual factors, both the absence of an acidic residue that is otherwise important for the CYP catalytic cycle and use of the dedicated Fd_{GA}. The evidence further indicates transient formation of 7β-ol-KA and use of a semipinacol mechanism for the ring contraction reaction. Given the use of such a carbocation-based mechanism also has been suggested for the functionally equivalent CYPs from plant and fungi (12), it will be of interest to determine the utilized mechanism as well as enzymatic structure–function relationships underlying the ability of these diverse, functionally equivalent CYPs to carry out this unusual ring contraction reaction.

Materials and Methods

Cloning of *Et*CYP114, *Et*Fd_{GA}, and *Bj*Fd_{GA} Constructs. *Et*CYP114 and *Et*Fd_{GA} from *E. tracheiphila* were amplified from previously described constructs (18) using Q5 Hot Start High-Fidelity DNA polymerase (NEB), and the primers are given in *SI Appendix*, Table S2. The forward primer was designed to add an alanine, six histidines, and a glycine after the initial methionine to the N terminus to enable facile purification. The reverse primer included a stop codon at the 3′-end so that the His-tag of pET101 (Invitrogen) is omitted. The resulting PCR product was cloned into the vector according to the product manual. A synthetic gene for *Et*Fd_{GA}, codon optimized for expression in *E. coli*, with the addition of an alanine, six histidines, and a glycine after the initial methionine, was also purchased (GeneArt, Thermo Fisher Scientific), and this was cloned into pENTR/SD/D-TOPO and subsequently pCDFDuet1-DEST. Fusion of *Et*CYP114 and *Et*Fd_{GA} was carried out via initial amplification of both genes (native *Et*FdGA) using Q5 Hot Start High-Fidelity DNA polymerase (NEB), which were gel purified and used as the template for another round of PCR, with introduction of the linker sequence, HAQAAAEVRVVVDQ, as found in *Rhizobium etli* CFN 42 with a 21 bp sequence overlap. The resulting PCR fragments were gel purified and equal molar amounts were combined for a third round of PCR with a forward primer for EtCYP114 and a reverse primer for *Et*Fd_{GA} only. The PCR product was gel purified and cloned into pET100 and pET101 using the CACC sequence included in the forward primer. The *Et*Fd_{GA} reverse primer included a stop codon; therefore, *Et*CYP114–Fd_{GA} fusion in pET100 has an N-terminal His-tag, while *Et*CYP114–Fd_{GA} fusion in pET101 does not a have a tag for purification. *Et*CYP114 or *Et*CYP114–Fd_{GA} fusion mutants were constructed using the Q5 site–directed mutagenesis kit (NEB), and primers are given in *SI Appendix*, Table S2. All constructs were verified by full-gene sequencing.

A synthetic gene for *Bj*Fd_{GA}, codon optimized for expression in *E. coli*, was purchased (GeneArt, Thermo Fisher Scientific), with the addition of six histidine residues at the C terminus and cloned into pDEST14 for protein purification purposes and into pCDFDuet1-DEST for metabolic engineering experiments. Additionally, a synthetic gene for the fusion of *Et*CYP114 and *Bj*Fd_{GA}, again codon optimized for expression in *E. coli*, was also purchased (GeneArt, Thermo Fisher Scientific) and cloned into pDEST14. All synthetic gene sequences (*Et*Fd, *Bj*Fd_{GA}, and *Et*CYP114–*Bj*Fd_{GA}) are shown in *SI Appendix*.

Expression and Purification. The expression vectors for *Et*CYP114, *Et*Fd_{GA}, and *Bj*Fd_{GA} described above, along with that previously described for *Et*FdR (26), were transformed into *E. coli* BL21* (Invitrogen). Starter cultures of 50 mL liquid NZY medium (10 g/L NaCl, 10 g/L casein, 5 g/L yeast extract, 1 g/L MgSO4 (anhydrous), pH 7.0) with 50 μg/mL carbenicillin were inoculated from 3 individual colonies and grown for 3 d at 18 °C with constant shaking at 180 rpm. Twenty milliliters of starter cultures was used to inoculate 1 L NZY (for *Et*CYP114, *Et*CYP114:A261D, *Et*FdR, *Et*Fd_{GA}) or 2xYT (16 g/L tryptone; 10 g/L yeast extract; 5 g/L NaCl; pH 6.8; for *Bj*Fd_{GA}) including 50 μg/mL carbenicillin, which were grown at 18 °C with constant shaking at 180 rpm until an OD_{600} of 0.8 (*Et*CYP114, *Et*CYP114:A261D, and *Bj*Fd_{GA}) or 0.6 (*Et*FdR and *Et*Fd_{GA}) was reached. The culture was then induced with 1 mM IPTG and, for cultures expressing *Et*CYP114, 1 mM aminolevulinic acid, 1 mM riboflavin, and 0.1 mM $FeCl_3$ were added. After 24 h (*Et*FdR, *Et*Fd_{GA}, and *Bj*Fd_{GA}) or 36 h (*Et*CYP114 and *Et*CYP114:A261D), the cells were harvested by centrifugation at 6,000 × g for 10 min. The cell pellets were resuspended in 10 mL of buffer (50 mM phosphate, pH 7.5, 10% (v/v) glycerol). Cell suspensions were then homogenized using an EmulsiFlex C-5 (Avestin, Canada) and DNase I (Sigma-Aldrich) was added. The lysate was centrifuged at 17,000 × g for 60 min. The clarified lysate was then added to 1 mL of Ni-NTA Agarose (Qiagen), imidazole (1 M solution in buffer) was added to a final concentration of 10 mM and this slurry incubated with gentle shaking at 4 °C for 1 h. The column was washed twice with 5 mL buffer, containing 20 mM imidazole and then 60 mM imidazole, before being eluted with 250 mM imidazole. The resulting protein was concentrated to 1 mL in Amicon® Ultra 4 mL Centrifugal Filters (MilliporeSigma), according to the instruction manual, with a molecular weight cutoff (MWCO) of 30 kDa for *Et*CYP114, *Et*CYP114:A261D, and *Et*FdR and 3 kDa for *Et*Fd_{GA} and *Bj*Fd_{GA}. *Et*CYP114, *Et*CYP114:A261D, *Et*FdR, and *Bj*Fd_{GA} were further purified by size-exclusion chromatography using an Äkta™ Start system (GE Healthcare Life Sciences) with a HiPrep 16/60 Sephacryl S-200 column (*Et*CYP114, *Et*CYP114:A261D, and *Et*FdR) or a HiLoad 16/60 Superdex 75pg column (*Bj*Fd_{GA}) (GE Healthcare Life Sciences). For *Et*FdR and *Bj*Fd_{GA}, the utilized buffer was 50 mM phosphate, pH 7.5, 10% (v/v) glycerol, while for *Et*CYP114 and *Et*CYP114:A261D, the buffer was 10 mM 3-(N-morpholino)-2-hydroxypropanesulfonic acid (MOPSO), pH 7.2, 5% (v/v) glycerol. Fractions containing the protein of interest were again concentrated using 3 to 30 kDa MWCO Amicon® Ultra 4 mL Centrifugal Filters and 0.1 mL aliquots in 1.5 mL Eppendorf tubes flash frozen by brief immersion in liquid nitrogen. *Et*CYP114 concentration was measured by optical absorbance at 280 nm, using the calculated extinction coefficient of 34,045 M^{-1} cm^{-1}, and BjFdGA concentration was measured using Bradford assay. *Et*Fd_{GA} was additionally purified in an anaerobic chamber (95% argon and 5% hydrogen, Coy Laboratories). DNase I was added to the cell suspension, and this was then deoxygenated by 5 cycles of vacuum followed by purging with oxygen-free argon in the air-lock of an anaerobic chamber, with homogenization via an EmulsiFlex C-5 (Avestin, Canada). The lysate was transferred to airtight centrifugation vessels and centrifuged outside the chamber as described above. After centrifugation, the closed vessel was reintroduced into the anaerobic chamber after 5 cycles of vacuum followed by purging with oxygen-free argon in the air-lock of the anaerobic chamber. His-tag purification was carried out in the anaerobic chamber as described above.

Crystallization and Data Collection. Apo crystals of *Et*CYP114 were grown by the hanging-drop vapor-diffusion method using 2.0 μL drops of buffered protein solution (10 to 15 mg/mL) mixed with equal volumes of the reservoir solution and incubated at 18 °C. Typical reservoir solutions were 20 to 25% PEG 3350 and 0.1 M Bis-Tris pH 5.5. Orthorhombic ($C222_1$) crystals typically grew within 2 wk. The crystals were then transferred to a cryoprotectant solution consisting of mother liquor supplemented with 20% (v/v) ethylene glycol, prior to immersion in liquid nitrogen. Crystal complexes of *Et*CYP114 with KA substrate were generated via cocrystallization as follows: purified *Et*CYP114 (45 mg/mL) was added to a glass vial with dried KA to reach a substrate concentration of 6 mM; the vial was kept on ice for 30 min with gentle swirling every 5 min. Using the hanging-drop vapor-diffusion method as described above, two crystal forms of the

*Et*CYP114+KA complex were observed. Crystal form 1, orthorhombic ($P2_12_12_1$), grew with reservoir solutions consisting of 16% PEG 3350, 0.1 M MES/Tris pH 5.6, 0.2 M $MgCl_2$ hexahydrate. Crystal form 2, monoclinic (C2), grew with reservoir solutions consisting of 25% PEG 4000, 0.1 M MES/Tris pH 5.6, 0.15 M ammonium sulfate and 10 mM cadmium chloride hydrate added as an additive. Cocrystals typically grew to full size within 2 wk. The cocrystals were transferred to a cryoprotectant solution as described above prior to immersion in liquid nitrogen.

Apo crystals of *Et*CYP114:A261D were grown by the hanging-drop vapor-diffusion method using 1.35 µL drops of buffered protein solution (23 mg/mL) mixed with 1.35 µL of the reservoir solution and incubated at 18 °C, and then 0.3 µL crystal seeds were added. Typical reservoir solutions were 25% PEG 3350, 0.1 M Bis-Tris pH 5.5, and 0.5% Polyvinylpyrrolidone K15. Orthorhombic ($C222_1$) crystals typically grew within 2 wk. The crystals were then transferred to a cryoprotectant solution consisting of mother liquor supplemented with 20% (v/v) ethylene glycol, prior to immersion in liquid nitrogen.

X-ray diffraction data for crystals of apo *Et*CYP114 and *Et*CYP114 cocrystallized with KA were collected using beamline 23-ID-D of the Advanced Photon Source, Argonne National Laboratory. Diffraction data for crystals of *Et*CYP114:A261D were collected using a Rigaku MicroMax 007 HF equipped with Rigaku RAXIS IV. Due to radiation damage, partial datasets from multiple crystals of *Et*CYP114:A261D were merged to generate a complete dataset for refinement. The datasets were processed using MOSFLM and AIMLESS from the CCP4 software suite (27–29).

Structure Determination, Model Building, and Refinement. Initial crystallographic phases for *Et*CYP114-apo crystals were determined by molecular replacement with Phaser from the CCP4 suite (30). A homology model of *Et*CYP114 was constructed with MODELLER (31) using the previously published structure of CYP107A1 [pdb id: 1Z8O (32)] as a template. Loops corresponding to residues 143 to 146, 191 to 196, 234 to 243, and 351 to 366 were removed from the homology model prior to molecular replacement. Morphing of the molecular replacement output model, using Morph model (33) in the Phenix software suite (34), was necessary prior to model rebuilding. The model was rebuilt and refined using Phenix. As needed, Coot (35) was used for graphical map inspection and manual rebuilding of atomic models. The crystallographic model of EtCYP114-apo was used as the search template for molecular replacement of the *Et*CYP114+KA complex structures. Rebuilding and refinement of *Et*CYP114+KA structures proceeded as described above, although model morphing was not necessary. The crystallographic model of *Et*CYP114-apo was used as the search template for molecular replacement of the *Et*CYP114+KA complex and *Et*CYP114:A261D structures. Rebuilding and refinement of *Et*CYP114+KA and *Et*CYP114:A261D structures also proceeded using Phenix. As needed, Coot (35) was used for graphical map inspection and manual rebuilding of atomic models. Molecular visualizations were generated with PyMOL and Ligplot+ (36), as indicated.

UV–Vis Spectroscopy. Spectral binding assays were carried out as previously described (37). Briefly, purified *Et*CYP114 or *Et*CYP114:A261D was diluted in the same buffer (10 mM MOPSO, pH 7.2, 5% (v/v) glycerol) so that absorbance at 417 nm was 0.6 to 0.7. Spectra were collected from 300 to 700 nm on a Cary 50 UV–Vis spectrometer (Varian) at a scan rate of 60 nm per minute. Substrates were added stepwise from a stock solution of 0.1 or 1 mg/mL dissolved in methanol (ethanol in the case of *ent*-kaurene). Methanol or ethanol was added to *Et*CYP114 as a control for spectral shifts originating from the solvent alone, with no changes in the UV–Vis spectrum observed with up to 5% methanol/ethanol (v/v). K_d values for individual binding curves were calculated using plots of the added substrate concentration versus the induced spectral shifts, and the curves were then fitted using the model for tight binding ligands with the following formula.

$$A_{obs} = \left(\frac{A_{max}}{2 * E_t}\right) * \left(S + E_t + K_d\right) - \sqrt{\left(S + E_t + K_d\right)^2 - \left(4 * S * E_t\right)}.$$

The mean and SE were calculated from three individual experiments. The affinity of 7β-ol-KA was further investigated by titration into a sample already containing 5 µM KA, with K_i determined from the IC_{50} of the concentration versus reverse spectral shift (38).

*Et*FdGA purified under anaerobic conditions was transferred immediately after elution from the Ni–NTA column with 50 mM phosphate buffer, pH 7.5, with 10% glycerol and 250 mM imidazole into an airtight cuvette (semi-micro rectangular cell with screw cap from Starna Cells). Spectra were collected on a Cary 50 UV–Vis spectrometer (Varian) at a scan rate of 60 nm per minute from 300 to 600 nm. Pure oxygen was injected into the cuvette using a syringe and the cuvette was inverted 3 times before the postoxygen exposure spectrum was collected.

Purified *Bj*Fd_{GA} after size-exclusion purification was transferred into a cuvette (semi-micro rectangular cell with screw cap from Starna Cells) containing 50 mM phosphate buffer, pH 7.5, with 10% glycerol. Spectra were collected on a Cary 50 UV–Vis spectrometer (Varian) at a scan rate of 60 nm per minute from 300 to 600 nm. The ferredoxin solution was reduced by the gradual addition of saturated sodium dithionite after recording the oxidized spectrum.

In Vivo Enzyme Activity of *Et*CYP114. *Et*CYP114 constructs were transformed into *E. coli* BL21* (Invitrogen). For separate coexpression with *Et*CYP114, the compatible pCDFDuet1-DEST::*Et*Fd_{GA} construct was used. Starter cultures of 5 mL liquid NZY with 50 µg/mL carbenicillin (plus 25 µg/mL spectinomycin for coexpression) were inoculated from three individual colonies and grown for 2 d at 18 °C with constant shaking at 180 rpm. For the main culture, 0.5 mL of the starter culture was used to inoculate 25 mL cultures of liquid TB medium (12 g/L casein, 24 mL/L yeast, 4 mL glycerol, 50 mM phosphate buffer, pH 7.0) with 50 µg/mL carbenicillin, which were grown with continuous shaking at 180 rpm at 18 °C until they reached an OD_{600} of 0.6. These cultures were then induced with 1 mM IPTG, and 1 mM aminolevulinic acid, 1 mM riboflavin, and 0.1 mM $FeCl_3$ were added to the culture along with 50 µg of the relevant substrate. Products were extracted from these cultures after 3 d, with acidification to pH 2 with hydrochloric acid, addition of 50 mL of a 1:1 mixture of hexanes and ethyl acetate, gentle swirling, and phase separation. The resulting organic extract was evaporated to dryness; the residue was methylated with diazomethane and, after reevaporation, dissolved in hexane for GC–MS analysis as previously described (18).

In Vitro Enzyme Assays. For in vitro activity assays, 0.01 mL each of purified *Et*CYP114, *Et*Fd_{GA}, or spinach ferredoxin (Sigma-Aldrich) and *Et*FdR (all at 1 mg/mL in buffer 1) were diluted with 1.5 mL of 50 mM phosphate, pH 7.5, 10% glycerol in 4 mL clear glass vials, and KA and NADPH were added to final concentrations of 20 µM and 60 µM, respectively. When H_2O_2 or *t*BuOOH was used as exogenous oxidant, no NADPH, *Et*FdR, or Fd was added, instead H_2O_2 was added to a final concentration of 60 µM or *t*BuOOH to a final concentration of 100 µM. The vial was sealed with a Teflon septum and incubated for 12 h at 25 °C.

For *Bj*Fd_{GA} in vitro activity assays, purified 10 µL *Et*CYP114 (35 mg/mL), 100 µL *Bj*Fd_{GA} (1 mg/mL) or 20 µL spinach ferredoxin (1 mg/mL; Sigma-Aldrich), and 10 µL spinach FdR (15U/mg; Sigma-Aldrich) were diluted with 0.5 mL of 50 mM phosphate, pH 7.5, 10% glycerol in 4 mL clear glass vials, and KA (5 µg) or 7-ol-KA (15 µg) and excess NADPH were added. The vial was sealed with a Teflon septum and incubated for 12 h at 25 °C.

The assay was acidified with hydrochloric acid to pH 2 and extracted 3 times with 2 mL of a 1:1 mixture of hexanes and ethyl acetate. The resulting organic extract was evaporated to dryness; the residue was methylated with diazomethane and, after reevaporation, dissolved in hexane for GC–MS analysis as previously described (18).

Data, Materials, and Software Availability. Protein crystal data have been deposited in PDB (8FIB; 8FIC; 8FID; 8FIE) (39–42).

ACKNOWLEDGMENTS. This work was supported by a grant from the NIH (GM131885) to R.J.P., along with a postdoctoral fellowship to R.N. from the Deutsche Forschungsgemeinschaft NA 1261/1-2. We would like to thank Prof. Alan DiSpirito for use of an anaerobic chamber. This research used resources of the Advanced Photon Source, a U.S. Department of Energy (DOE) Office of Science User Facility operated for the DOE Office of Science by Argonne National Laboratory under Contract No. DE-AC02-06CH11357. Specifically, general user proposals GUP-48455 and GUP-58384 supported collection of X-ray diffraction data at the National Institute of General Medical Sciences and National Cancer Institute Structural Biology Facility) beamline 23-ID-D at the Advanced Photon Source, Argonne National Laboratory.

Author affiliations: [a]Roy J. Carver Department of Biochemistry, Biophysics and Molecular Biology, Iowa State University, Ames, IA 50011; and [b]Macromolecular X-ray Crystallography Facility, Iowa State University, Ames, IA 50011

Author contributions: R.N., L.E.A., and R.J.P. designed research; R.N., L.E.A., and C.E.S. performed research; R.N., L.E.A., C.E.S., and R.J.P. analyzed data; and R.N. and R.J.P. wrote the paper.

1. D. R. Nelson, Cytochrome P450 diversity in the tree of life. *Biochim. Biophys. Acta Proteins Proteom.* **1866**, 141–154 (2018).
2. D. C. Lamb, M. R. Waterman, Unusual properties of the cytochrome P450 superfamily. *Philos. Trans. R. Soc. Lond. B Biol. Sci.* **368**, 20120434 (2013).
3. P. R. Ortiz de Montellano, Hydrocarbon hydroxylation by cytochrome P450 enzymes. *Chem. Rev.* **110**, 932–948 (2010).
4. C. M. Krest *et al.*, Reactive intermediates in cytochrome p450 catalysis. *J. Biol. Chem.* **288**, 17074–17081 (2013).
5. F. P. Guengerich, Cataloging the repertoire of nature's Blowtorch, P450. *Chem. Biol.* **16**, 1215–1216 (2009).
6. P. J. Mak, I. G. Denisov, Spectroscopic studies of the cytochrome P450 reaction mechanisms. *Biochim. Biophys. Acta Proteins Proteom.* **1866**, 178–204 (2018).
7. T. L. Poulos, E. F. Johnson, "Structures of cytochrome P450 enzymes" in *Cytochrome P450: Structure, Mechanism, and Biochemistry*, P. R. Ortiz de Montellano, Ed. (Springer, Switzerland, 2015).
8. I. G. Denisov, S. G. Sligar, "Activation of molecular oxygen in cytochromes P450" in *Cytochrome P450: Structure, Mechanism, and Biochemistry*, P. R. Ortiz de Montellano, Ed. (Springer, Switzerland, 2015).
9. K. Hiroya, Y. Murakami, T. Shimizu, M. Hatano, P. R. Ortiz de Montellano, Differential roles of Glu318 and Thr319 in cytochrome P450 1A2 catalysis supported by NADPH-cytochrome P450 reductase and tert-butyl hydroperoxide. *Arch. Biochem. Biophys.* **310**, 397–401 (1994).
10. F. P. Guengerich, A. W. Munro, Unusual cytochrome p450 enzymes and reactions. *J. Biol. Chem.* **288**, 17065–17073 (2013).
11. M. C. Tang, Y. Zou, K. Watanabe, C. T. Walsh, Y. Tang, Oxidative cyclization in natural product biosynthesis. *Chem. Rev.* **117**, 5226–5333 (2017).
12. P. R. Ortiz de Montellano, S. D. Nelson, Rearrangement reactions catalyzed by cytochrome P450s. *Arch. Biochem. Biophys.* **507**, 95–110 (2011).
13. P. Hedden, V. Sponsel, A century of gibberellin research. *J. Plant Growth Regul.* **34**, 740–760 (2015).
14. R. Bari, J. D. Jones, Role of plant hormones in plant defence responses. *Plant Mol. Biol.* **69**, 473–488 (2009).
15. R. S. Nett *et al.*, Elucidation of gibberellin biosynthesis in bacteria reveals convergent evolution. *Nat. Chem. Biol.* **13**, 69–74 (2017).
16. M. C. Gregory, I. G. Denisov, Y. V. Grinkova, Y. Khatri, S. G. Sligar, Kinetic solvent isotope effect in human P450 CYP17A1-mediated androgen formation: Evidence for a reactive peroxoanion intermediate. *J. Am. Chem. Soc.* **135**, 16245–16247 (2013).
17. R. Nagel, J. Bieber, M. G. Schmidt-Dannert, R. S. Nett, R. J. Peters, A third class: Functional gibberellin biosynthetic operon in beta-proteobacteria. *Front. Microbiol.* **9**, 2916 (2018).
18. R. Nagel, R. J. Peters, Investigating the phylogenetic range of gibberellin biosynthesis in bacteria. *Mol. Plant Microbe Interact.* **30**, 343–349 (2017).
19. R. Nagel *et al.*, An operon for production of bioactive gibberellin A4 phytohormone with wide distribution in the bacterial rice leaf streak pathogen *Xanthomonas oryzae* pv. *oryzicola*. *New Phytol.* **214**, 1260–1266 (2017).
20. R. S. Nett, J. S. Dickschat, R. J. Peters, Labeling studies clarify the committed step in bacterial gibberellin biosynthesis. *Org. Lett.* **18**, 5974–5977 (2016).
21. D. M. Hershey, X. Lu, J. Zi, R. J. Peters, Functional conservation of the capacity for *ent*-kaurene biosynthesis and an associated operon in certain rhizobia. *J. Bacteriol.* **196**, 100–106 (2014).
22. Y. Tatsukami, M. Ueda, Rhizobial gibberellin negatively regulates host nodule number. *Sci. Rep.* **6**, 27998 (2016).
23. F. P. Guengerich, M. R. Waterman, M. Egli, Recent structural insights into cytochrome P450 function. *Trends Pharmacol. Sci.* **37**, 625–640 (2016).
24. T. L. Poulos, A. H. Follmer, Updating the paradigm: Redox partner binding and conformational dynamics in cytochromes P450. *Acc. Chem. Res.* **55**, 373–380 (2022).
25. M. Mizutani, F. Sato, Unusual P450 reactions in plant secondary metabolism. *Arch. Biochem. Biophys.* **507**, 194–203 (2011).
26. R. Nagel, R. J. Peters, Diverging mechanisms: Cytochrome-P450-catalyzed demethylation and gamma-Lactone formation in bacterial gibberellin biosynthesis. *Angew. Chem. Int. Ed. Engl.* **57**, 6082–6085 (2018).
27. T. G. G. Battye, L. Kontogiannis, O. Johnson, H. R. Powell, A. G. W. Leslie, iMOSFLM: A new graphical interface for diffraction-image processing with MOSFLM. *Acta Crystallogr. D Biol. Crystallogr.* **67**, 271–281 (2011).
28. P. R. Evans, G. N. Murshudov, How good are my data and what is the resolution? *Acta Crystallogr. D Biol. Crystallogr.* **69**, 1204–1214 (2013).
29. M. D. Winn *et al.*, Overview of the CCP4 suite and current developments. *Acta Crystallogr. D Biol. Crystallogr.* **67**, 235–242 (2011).
30. A. J. McCoy *et al.*, Phaser crystallographic software. *J. Appl. Crystallogr.* **40**, 658–674 (2007).
31. A. Sali, T. L. Blundell, Comparative protein modelling by satisfaction of spatial restraints. *J. Mol. Biol.* **234**, 779–815 (1993).
32. S. Nagano, J. R. Cupp-Vickery, T. L. Poulos, Crystal structures of the ferrous dioxygen complex of wild-type cytochrome P450eryF and its mutants, A245S and A245T: Investigation of the proton transfer system in P450eryF. *J. Biol. Chem.* **280**, 22102–22107 (2005).
33. T. C. Terwilliger *et al.*, Improved crystallographic models through iterated local density-guided model deformation and reciprocal-space refinement. *Acta Crystallogr. D Biol. Crystallogr.* **68**, 861–870 (2012).
34. P. D. Adams *et al.*, PHENIX: A comprehensive Python-based system for macromolecular structure solution. *Acta Crystallogr. D Biol. Crystallogr.* **66**, 213–221 (2010).
35. P. Emsley, K. Cowtan, Coot: Model-building tools for molecular graphics. *Acta Crystallogr. D Biol. Crystallogr.* **60**, 2126–2132 (2004).
36. R. A. Laskowski, M. B. Swindells, LigPlot+: Multiple ligand-protein interaction diagrams for drug discovery *J. Chem. Inf. Model.* **51**, 2778–2786 (2011).
37. R. Nagel, R. J. Peters, Probing the specificity of CYP112 in bacterial gibberellin biosynthesis. *Biochem. J.* **475**, 2167–2177 (2018).
38. Y. Cheng, W. H. Prusoff, Relationship between the inhibition constant (K1) and the concentration of inhibitor which causes 50 per cent inhibition (I50) of an enzymatic reaction. *Biochem. Pharmcol.* **22**, 3099–3109 (1973).
39. R. Nagela, L. E. Alexandera, C. E. Stewart Jr., R. J. Peters, *Et*CYP114 (apo). *Protein Data Bank*. https://csb.org/structure/unreleased/8FIB. Deposited 16 December 2022.
40. R. Nagela, L. E. Alexandera, C. E. Stewart Jr., R. J. Peters, *Et*CYP114+*ent*-kaurenoic acid (crystal form 1). *Protein Data Bank*. https://csb.org/structure/unreleased/8FIC. Deposited 16 December 2022.
41. R. Nagela, L. E. Alexandera, C. E. Stewart Jr., R. J. Peters, *Et*CYP114+*ent*-kaurenoic acid (crystal form 2). *Protein Data Bank*. https://csb.org/structure/unreleased/8FID. Deposited 16 December 2022.
42. R. Nagela, L. E. Alexandera, C. E. Stewart Jr., R. J. Peters, *Et*CYP114:A261D (apo). *Protein Data Bank*. https://csb.org/structure/unreleased/8FIE. Deposited 16 December 2022.